Supplementary information

Stage-Dominated Thermal Runaway in Sulfide ASSBs: Decoupled Electrochemical Ignition and Chemical Cascades

Yuhan Wu[1, 2, #], Shu Zhang[1, 3, 4, #], Youlong Sun[1, 2, #], Lang Huang[1, 2, 3, 4, *], Jiahao Xu[1, 2], Chengao Liu[1, 2], Shanshan Zhu[1, 2], Zhaoxuan Jiang[1, 2], Tianyu Gong[1], Lingxiang Guo[1], Longfei Cui[1], Tao Liu[1], Jiangwei Ju[1, 2, 3, 4], Guanglei Cui[1, 2, 3, 4, *]

[1]Qingdao Industrial Energy Storage Research Institute, Qingdao Institute of Bioenergy and Bioprocess Technology, Chinese Academy of Sciences, Qingdao 266101, China.

[2]University of Chinese Academy of Sciences, Beijing 100049,China.

[3]Shandong Energy Institute, Qingdao 266101, China.

[4]Qingdao New Energy Shandong Laboratory, Qingdao 266101, China.

[#]These authors contributed equally: Yuhan Wu, Shu Zhang, Youlong Sun.

E-mail: huanglang@qibebt.ac.cn, cuigl@qibebt.ac.cn.

1.1. Materials preparation.

Bare $LiNi_{0.8}Co_{0.1}Mn_{0.1}O_2$, Al_2O_3-coated $LiNi_{0.8}Co_{0.1}Mn_{0.1}O_2$, VGCF, indium, and silicon are acquired from Guangdong Canrd New Energy Technology Co., Ltd. LGPS is sourced from Hefei Kejing MaterialTechnology Co., Ltd. LSPSC is purchased from Shanghai Xianxin New Materials Technology Co., Ltd. Li_2S is acquired from Alfa Aesar Chemical Co., Ltd. LiCl, P_2S_5, and GeS_2 are purchased from Macklin Co., Ltd. LPSC is synthesized through a mechanochemical method. A stoichiometric mixture of Li_2S, P_2S_5, and LiCl is ball-milled at 600 rpm for 24 hours (h). The resultant mixture is then compressed into pellets, which are subsequently placed within a quartz tube. These pellets undergo annealing at 550 ℃ for 5 h, followed by a gradual cooling process to room temperature. Afterward, the pellets are pulverized using an agate mortar to achieve the Li_6PS_5Cl powder. All procedures are conducted under argon. β-L_3PS_4 is synthesized through a mechanochemical method. A stoichiometric mixture of Li_2S and P_2S_5 is ball-milled at 480 rpm for 48 h, followed by heating at 300 ℃ for 8 h in Ar. Li_4GeS_4 is synthesized through a mechanochemical method. A

stoichiometric mixture of Li_2S and GeS_2 is ball-milled at 600 rpm for 36 h, followed by heating at 500 ℃ for 6 h in Ar.

1.2. Electrode preparation.

For the preparation of composite cathode powders, cathode materials such as $LiNi_{0.8}Co_{0.1}Mn_{0.1}O_2$ and Al_2O_3-coated $LiNi_{0.8}Co_{0.1}Mn_{0.1}O_2$, SEs (such as LPSC, LGPS, LSPSC, and LGS), and VGCF powders are mixed in a weight ratio of 70:30:3, respectively. SE/VGCF (LPSC/VGCF, LGPS/VGCF, and LSPSC/VGCF) electrode composite powders are prepared through a mechanochemical method. A stoichiometric mixture of SE and VGCF in a weight ratio of 9:1 is ball-milled at 300 rpm for 2 h. The Li-In alloy is stored after the lithium foil and indium foil are pressed together. The $Li_{2.5}Si$ alloy is prepared by manually grinding the stoichiometric mixture of Si powders and lithium foil in a glovebox filled with an Ar atmosphere.

1.3. Electrochemical Characterization.

$LiNi_{0.8}Co_{0.1}Mn_{0.1}O_2$/LPSC/Li-In ASSBs are assembled for investigating the cycling performance of $LiNi_{0.8}Co_{0.1}Mn_{0.1}O_2$. The ASSB is assembled in a PEEK die (10 mm diameter). 100 mg LPSC powders are first pressed under a force of 1.6 tons as the electrolyte layer. Then the prepared composite cathode powders are added homogeneously on the top of the electrolyte layer and compressed under a force of 3.2 tons. In the end, Li-In alloy anode is added on the bottom of the LPSC layer and compressed for 2 min under a force of 0.4 tons. The stack pressure is 50 MPa during battery operation. The cycle performances are evaluated using a Neware battery test system (CT-4008Q, China) in the voltage range of 2.8−4.2 V (vs. Li^+/Li) at 0.1C and 30 ℃.

$LiNi_{0.8}Co_{0.1}Mn_{0.1}O_2$/LPSC/Li-In ASSBs are assembled for thermal runaway. The ASSBs are assembled in a PEEK die (20 mm diameter). 400 mg LPSC powders are first pressed under a force of 4 tons as the electrolyte layer. Then the prepared composite cathode powders are added homogeneously on the top of the electrolyte layer and compressed under a force of 10 tons. In the end, Li-In alloy anode is added on the bottom of the LPSC layer and compressed for 2 min under a force of 1.6 tons. The stack pressure is 50 MPa during battery operation. The cycle performances are

evaluated using a Neware battery test system (CT-4008Q, China) in the voltage range of 2.8−4.5 V (vs. Li^+/Li) at 0.05C and 30 ℃.

SE/VGCF (LPSC/VGCF, LGPS/VGCF, and LSPSC/VGCF)/LPSC/In half-cells are assembled to obtain the SEs after electrochemical decomposition. The half-cells are assembled in a PEEK die (20 mm diameter). 400 mg LPSC powders are first pressed under a force of 4 tons as the electrolyte layer. Then the prepared composite cathode powders are added homogeneously on the top of the electrolyte layer and compressed under a force of 10 tons. In the end, indium anode is added on the bottom of the LPSC layer and compressed for 2 min under a force of 1.6 tons. The stack pressure is 50 MPa during battery operation. The cycle performances are evaluated using a Neware battery test system (CT-4008Q, China) after charging to 4.5 V (vs. Li^+/Li) at 0.05C and 30 ℃.

LGS+$LiNi_{0.8}Co_{0.1}Mn_{0.1}O_2$/LPSC/$Li_{2.5}Si$ ASSB is assembled for investigating the cycling performance of the battery with LGS as an ionic conductor additive in the composite cathode. The ASSB is assembled in a PEEK die (10 mm diameter). 100 mg LPSC powders are first pressed under a force of 1.6 tons as the electrolyte layer. Then the prepared composite cathode powders are added homogeneously on the top of the electrolyte layer and compressed under a force of 3.2 tons. In the end, $Li_{2.5}Si$ alloy anode is added on the bottom of the LPSC layer and compressed for 2 min under a force of 4 tons. The stack pressure is 50 MPa during battery operation. The cycle performances are evaluated using a Neware battery test system (CT-4008Q, China). The assembled ASSBs are activated for 2 cycles in the voltage range of 2.4−4.2 V at 0.05C and 45 ℃, and then undergo charge-discharge cycling in the voltage range of 2.4−4.2 V at 0.5C and 45 ℃.

1.4. Materials characterization.

Accelerating Rate Calorimeter (ARC) and Ramp test of pouch cell and electrode-electrolyte are conducted with a BTC130 (HEL, England), equipped with a mass spectrum (MS, HPR-20, Hiden Analytical Ltd). The “Heat-Wait-Search” model starting temperature is 100 ℃ with a heating step of 10 ℃. The self-heating rate detection limit is 0.02 ℃ min^{-1} and thermal runaway criteria is 1 ℃ min^{-1}. The “Ramp”

model is heated with a heating rate of 5 ℃ min^{-1} up to 400 ℃. The electrode materials and SEs are carefully disassembled from ASSBs in an Ar-filled glove box. 200mg electrode materials are transferred into the small bomb chamber made of Hastelloy alloy for Ramp test, and the released gases are analyzed by MS. The Differential Scanning Calorimeter (DSC) measurement is conducted with a Netzsch DSC214 system from 20 ℃ to 500 ℃ with a heating rate of 5 ℃ min^{-1}. Samples, about 10.0 mg, are placed in the stainless steel high-pressure sealed crucible (100μL, NETZSCH, Germany). The weight ratio of active materials and electrolytes is set as NCM: SE = 7: 3. Scanning electron microscopy (SEM) images of cathode are taken by S-4800 field emission SEM (Hitachi, Japan), operated at 10 kV and element mapping test is conducted by 7593-H(Horiba, Japan). Lab-scale X-ray diffraction (XRD) measurements are conducted using a Rigaku SmartLab X-ray diffractometer equipped with Cu Kα radiation. Temperature-resolved X-ray diffraction with an external direct heating component from room temperature up to 400 ℃ at a heating rate of 1 ℃ min^{-1}, is tested from 10° to 70° with a scan speed of 10° min^{-1}. Raman measurements are conducted on a Thermo Scientific spectrometer (Raman Microscope DXR) equipped with a 532 nm laser. The surface chemistry of the materials is detected by X-ray photoelectron spectroscopy (XPS, Thermo Scientific ESCA Lab 250Xi). Time-of-flight secondary ion mass spectrometry (TOF-SIMS) measurements are performed in a negative mode with a 30 keV Bi^{3+} primary ion beam source. Transmission electron microscope (TEM, Talos F200X) and electron energy loss epectroscopy (EELS) are taken for a detailed structural analysis. The electron backscattered diffraction (EBSD) images are acquired with Oxford C-nano. The focused ion beam (FIB) technique can cut samples and expose the cross sections of samples for TEM. The cross section polisher (CP) technique can cut samples and expose the cross sections of samples for EBSD.

1.5. Calculation method

All first-principles calculations are performed using the plane-wave projector-augmented wave method, as implemented in the Vienna ab initio simulation package (VASP) within the MedeA technology platform[1-2]. The

Perdew−Burke−Ernzerhof (PBE) form of generalized gradient approximation (GGA) is chosen as the exchange−correlation potential[3]. PBE+U approach is performed to calculate accurate structural properties and electronic properties with spin polarization. The effective U value was set to 6.7, 4.2, and 4.9 eV for Ni, Mn, and Co, respectively[4]. The plane-wave energy cutoff of 520 eV was used for structural relaxation. The conjugated gradient method is utilized to optimize the geometry with the convergence threshold of 10^{-5} eV in energy and 0.01 eV/Å in force, respectively. The potential decomposition reactions at the interfaces were examined along the pseudobinary phase diagrams with varying fractions of reactants[5]. The interfacial reaction of the cathode with the electrolyte at elevated temperature were simulated by ab initio molecular dynamics (AIMD). The equations of motion were integrated with the Verlet algorithm using a time step of 2 fs, and micro canonical ensemble (NVE) was used to simulate the interfacial reaction from room temperature to 500 ℃. A plane-wave basis set with an energy cut-off of 520 eV and a 1 × 1 × 1 k-point mesh were used for the AIMD simulations. The AIMD simulations were performed for 2 ps.

1.6. References

[1] Kresse, G.; Hafner, J. Ab initio molecular-dynamics simulation of the liquid-metal-amorphous-semiconductor transition in germanium. *Phys Rev B Condens Matter*, **1994**, 49, 14251-14269.

[2] Bounar, Nedjemeddine; Benabbas, Abderrahim; Bouremmad, Farida, et al. Structure, microstructure and ionic conductivity of the solid solution LiTi2−xSnx(PO4)3. *Physica B*, **2012**, 407, 403-407.

[3] Perdew, John P.; Burke, Kieron; Ernzerhof, Matthias. Generalized Gradient Approximation Made Simple. *Phys. Rev. Lett.*, **1996**, 77, 3865-3868.

[4] Ou, X.; Liu, T.; Zhong, W., et al. Enabling high energy lithium metal batteries via single-crystal Ni-rich cathode material co-doping strategy. *Nat Commun*, **2022**, 13, 2319.

[5] Zhu, Yizhou; He, Xingfeng; Mo, Yifei. First principles study on electrochemical and chemical stability of solid electrolyte–electrode interfaces in all-solid-state Li-ion batteries. *J. Mater. Chem. A*, **2016**, 4, 3253-3266.

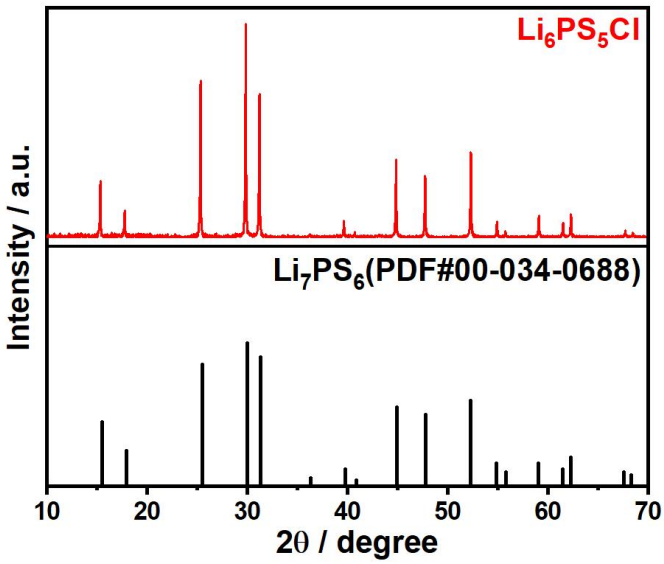

Figure S1. XRD patterns of the as-synthesized Li_6PS_5Cl samples.

The as-synthesized Li_6PS_5Cl samples are used as the electrolyte in ASSBs and as a conductive additive in the composite cathode (NMC811, LPSC, and VGCF in a weight ratio of 70:30:3).

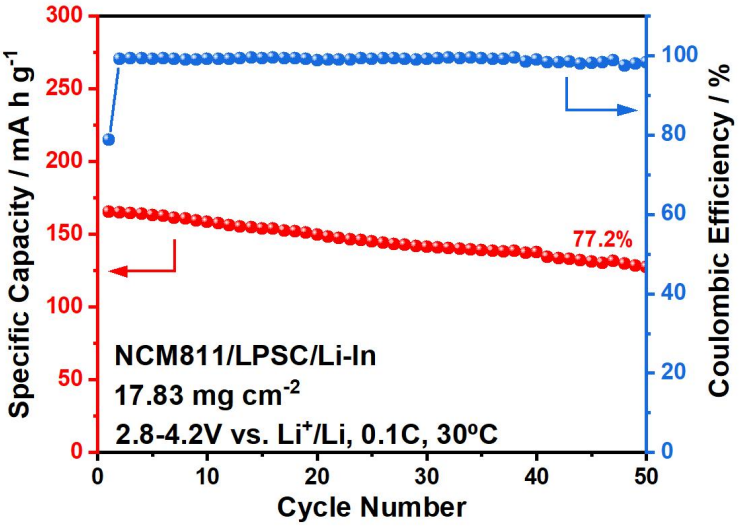

Figure S2. Typical cycle performance and coulombic efficiency of NCM811/LPSC/Li-In cells in the voltage range of 2.8−4.2 V (vs. Li^+/Li) at 0.1C and 30 ℃.

This experiment aims to evaluate the electrochemical performance of the self-assembled ASSBs.

The as-obtained cells delivered considerable cycling performance, with an initial discharge specific capacity of 165.1 $mAh \cdot g^{-1}$ and a significant capacity retention of 77.2% after 100 cycles.

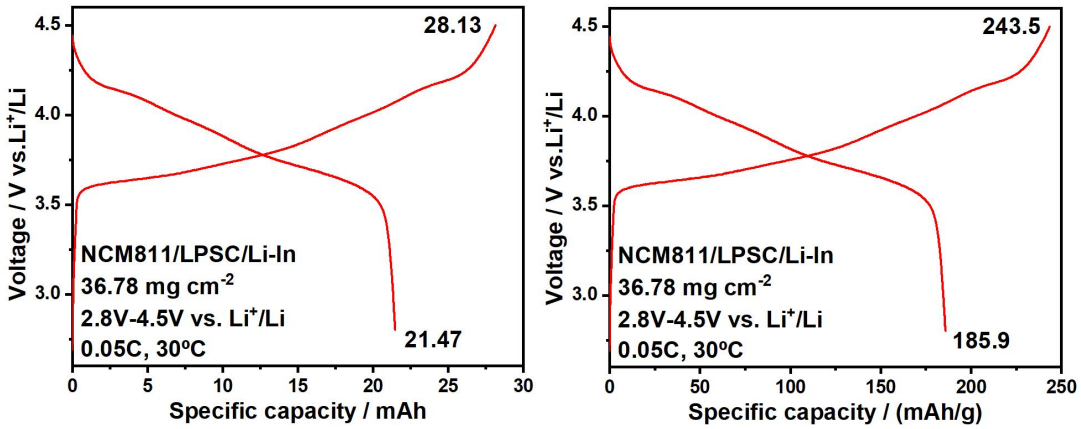

Figure S3. Typical charge-discharge profiles of NCM811/LPSC/Li-In cells in the voltage range of 2.8−4.5 V (vs. Li^+/Li) at 0.05C and 30 ℃.

The ASSBs obtained from this experiment are used for thermal runaway testing.

The as-obtained cells delivered an initial charge capacity of 28.13 mAh (243.5 $mAh \cdot g^{-1}$) and an initial discharge specific capacity of 21.47 mAh (185.9 $mAh \cdot g^{-1}$).

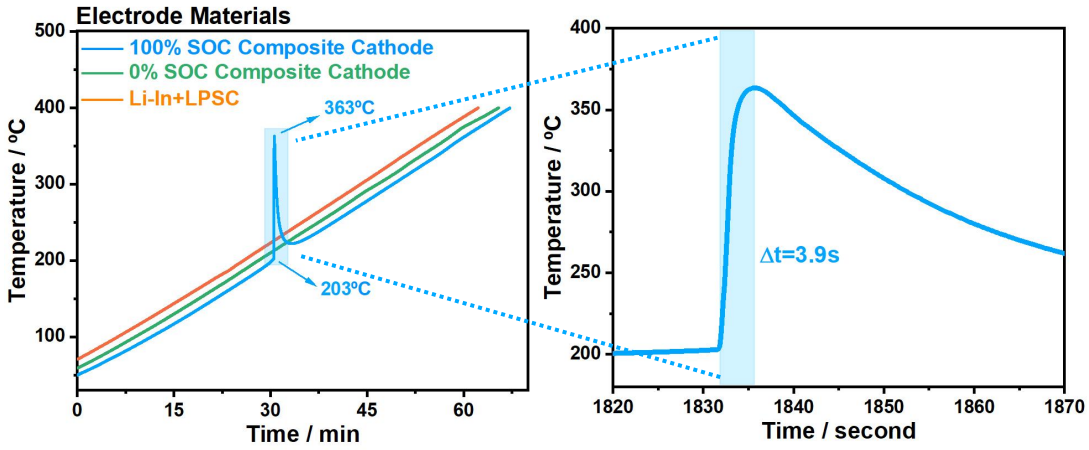

Figure S4. Adiabatic ramp test thermal profiles of electrode materials (anode and cathode) at a scanning rate of 5 ℃ min^{-1} in ARC.

This experiment aims to investigate the thermal runaway behavior of electrode materials under a constant heating rate of 5 ℃ min^{-1}.

The 100% SOC composite cathode (NMC811, LPSC, and VGCF in a weight ratio of 70:30:3) exhibited severe self-heating, with the sample temperature rapidly increases to 363 ℃ within 3.9 seconds at 203 ℃, indicating that thermal abuse can trigger thermal runaway in composite cathode.

Figure S5. Typical images of the 100% SOC composite cathode pellets (NMC811, LPSC, and VGCF in a weight ratio of 70:30:3) for thermal runaway driven by mechanical abuse under inert atmospheres.

This experiment aims to investigate the thermal runaway of the 100% SOC composite cathode under mechanical abuse conditions.

Grinding the 100% SOC composite cathode led to violent burning, demonstrating that mechanical abuse can also trigger thermal runaway.

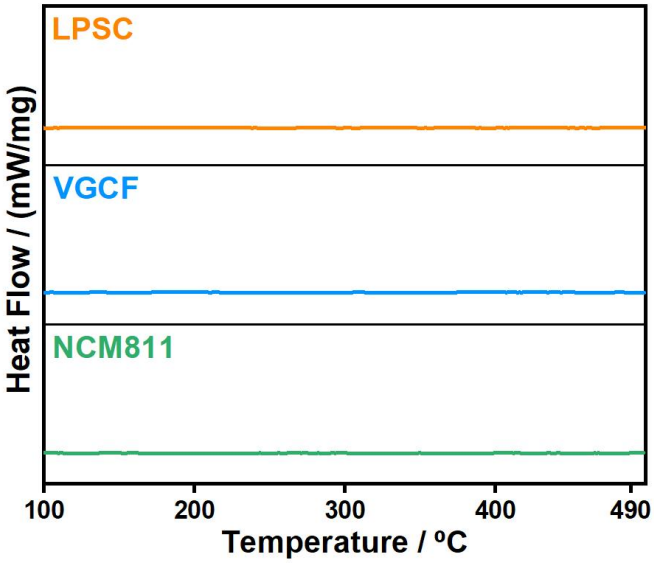

Figure S6. DSC profiles of LPSC, VGCF, and NCM811 samples.

This experiment aims to demonstrate that LPSC, VGCF, and NCM811 all exhibit excellent thermal stability.

The three pristine samples without mixing exhibited no heat absorption or release, confirming their inherent high thermal stability

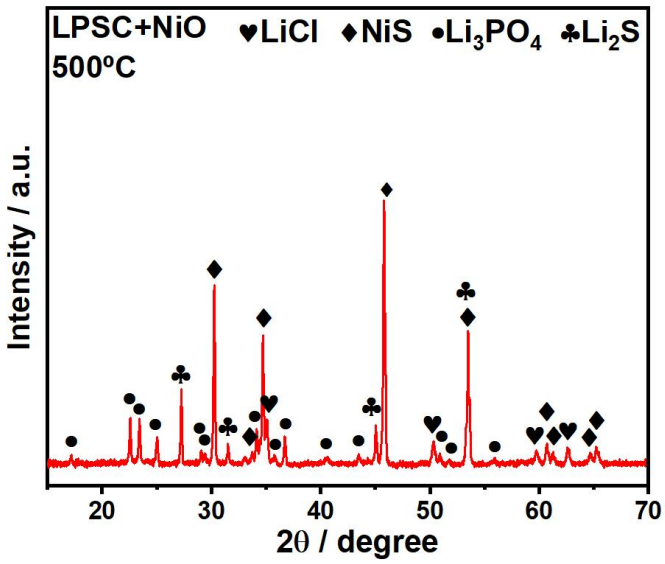

Figure S7. XRD patterns of LPSC with NiO in a 1:1 mass ratio after heating at 500 ℃.

The aim of this experiment is to confirm that the second exothermic reaction in the pristine composite cathode involves the interactions between transition metal oxides and LPSC.

The heating of LPSC with NiO resulted in the formation of NiCl, NiS, Li_3PO_4, and Li_2S. The formation of transition metal sulfides proved the validity of this conclusion.

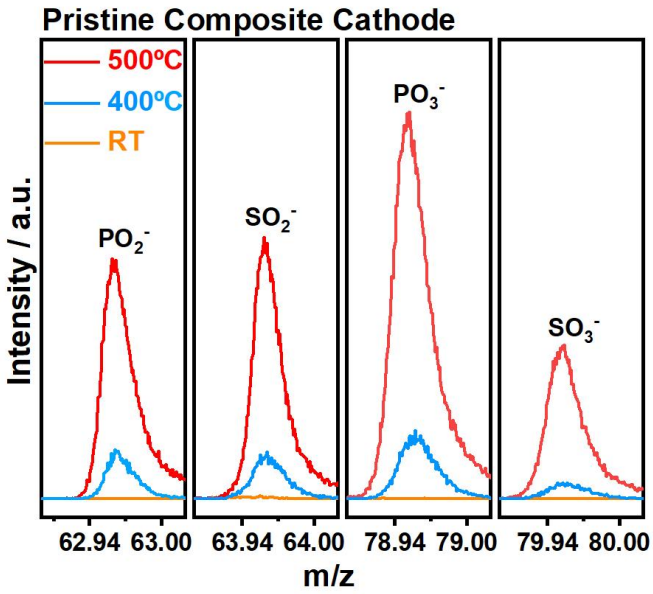

Figure S8. TOF-SIMS for the pristine composite cathode (NMC811, LPSC, and VGCF in a weight ratio of 70:30:3) at room temperature (RT, 25 ℃), 400 ℃, and 500 ℃.

To determine the exothermic reactions of NCM811 and LPSC in the pristine composite cathode, we conduct tests by heating the samples to various temperatures.

The m/z at 62.96, 63.96, 78.95, and 79.95 correspond to PO_2^-, SO_2^-, PO_3^-, and SO_3^-. At 400 ℃, the generation of PO_2^-, SO_2^-, PO_3^-, and SO_3^- indicated that the interfacial reactions are accompanied by the formation of P-O and S-O bonds. Upon further heating to 500 ℃, the increased intensity of these signals suggested further generation of P-O and S-O bonds.

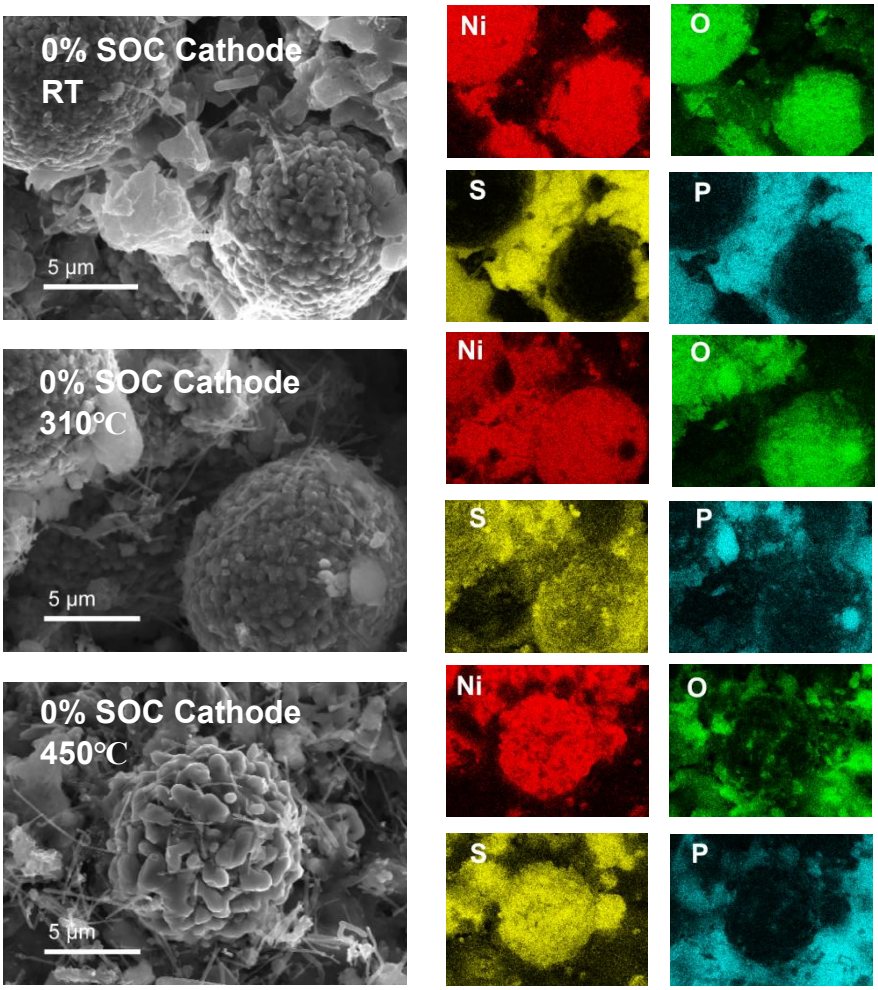

Figure S9. Typical surface SEM images and Ni, O, S, and P mapping results of the 0% SOC composite cathode (NMC811, LPSC, and VGCF in a weight ratio of 70:30:3) after heating at room temperature (RT, 25 ℃), 310 ℃, and 450 ℃.

To determine the exothermic reactions of the 0% SOC composite cathode, we conduct tests by heating the samples to various temperatures.

After heating at 310 ℃, it was observed by SEM imaging that the diffusion of sulfur (S) into NCM811, indicating the decomposition of the interphase components. After heating at 450 ℃, strong presence of Ni and S were observed in NCM811, while strong P and O were found in LPSC, indicating the complete occurrence of the interfacial reactions between NCM811 and LPSC.

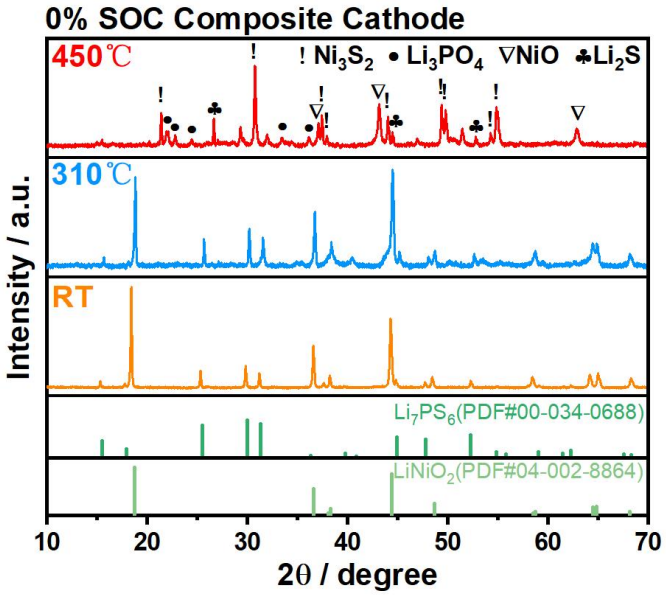

Figure S10. XRD spectra for the 0% SOC composite cathode (NMC811, LPSC, and VGCF in a weight ratio of 70:30:3) measured at room temperature (RT, 25 ℃), 310 ℃, and 450 ℃.

To determine the exothermic reactions of the 0% SOC composite cathode, we conduct tests by heating the samples to various temperatures.

When heated to 310 ℃, no significant changes occurred, suggesting that no reaction occurred between NCM811 and LPSC. Upon heating to 450 ℃, the characteristic peaks of NCM811 and LPSC disappeared, while interfacial reactions products such as Ni_3S_2, Li_3PO_4, NiO, and Li_2S emerged. These findings indicate that the reactions between NCM811 and LPSC only occur during the second exothermic reaction, without involvement in the first exothermic event.

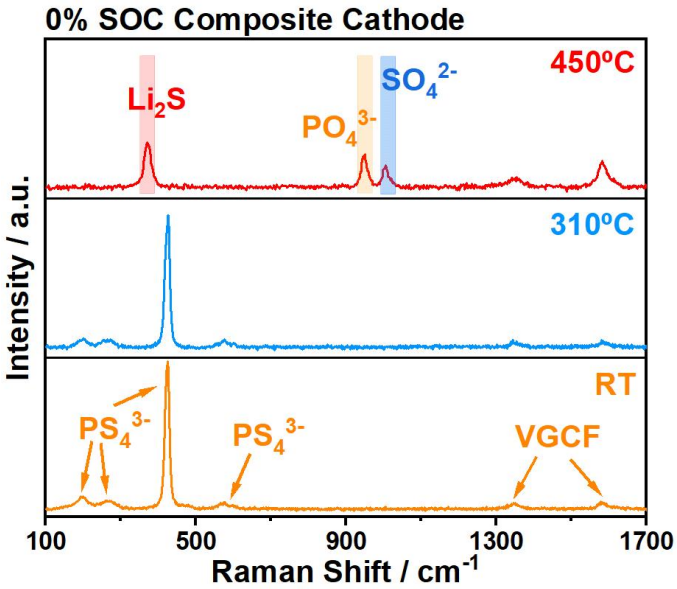

Figure S11. Raman profile of the 0% SOC composite cathode (NMC811, LPSC, and VGCF in a weight ratio of 70:30:3) after heating at room temperature (RT, 25 ℃), 310 ℃, and 450 ℃.

To determine the exothermic reactions of the 0% SOC composite cathode, we conduct tests by heating the samples to various temperatures.

For the 0% SOC composite cathode, no significant changes were observed when heated to 310°C, indicating that no reaction occurred between NCM811 and LPSC. Upon heating to 450 ℃, the characteristic peaks of NCM811 and LPSC disappeared, while interphase products such as Li_2S, PO_4^{3-}, and SO_4^{2-} emerged. These findings indicate that the reactions between NCM811 and LPSC only occur during the second exothermic reaction, without involvement in the first exothermic event.

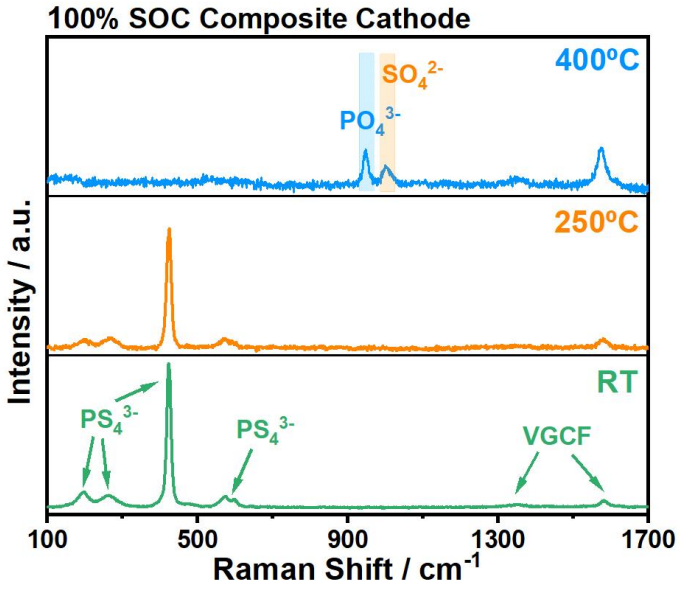

Figure S12. Raman profile of the 100% SOC composite cathode (NMC811, LPSC, and VGCF in a weight ratio of 70:30:3) after heating at room temperature (RT, 25 ℃), 250 ℃, and 400 ℃.

To determine the exothermic reactions of the 100% SOC composite cathode, we conduct tests by heating the samples to various temperatures.

For the 100% SOC composite cathode, no significant changes were observed when heated to 250°C, indicating that no reaction occured between NCM811 and LPSC. Upon heating to 450 ℃, the characteristic peaks of NCM811 and LPSC disappeared, while interphase products such as Li_2S, PO_4^{3-}, and SO_4^{2-} emerged, indicating the complete occurrence of the interfacial reactions between NCM811 and LPSC.

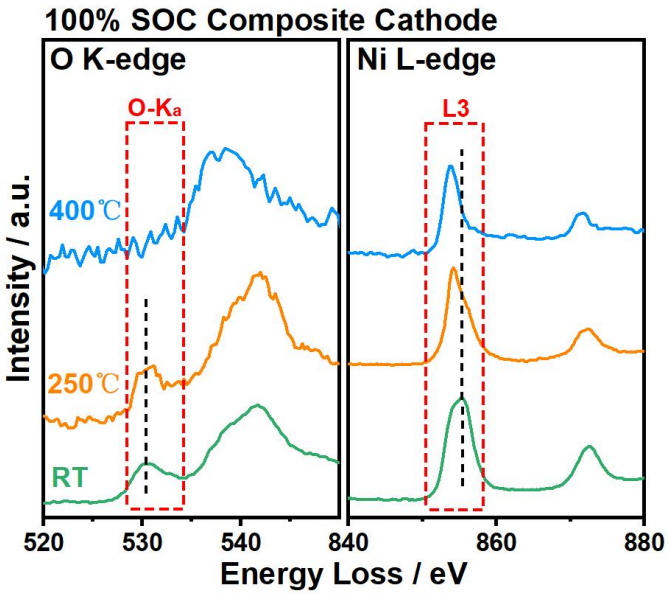

Figure S13. EELS spectrum of the 100% SOC composite cathode (NMC811, LPSC, and VGCF in a weight ratio of 70:30:3) after heating at room temperature (RT, 25 ℃), 250 ℃, and 400 ℃.

The aim of this experiment is to determine the exothermic reactions in the 100% SOC composite cathode by analyzing the changes in the valence states of transition metal elements.

At 250 ℃, the shift of the O K-edge pre-edge peak (527-534 eV, O-Ka) to higher energy loss and the Ni L-edge peak (852-858 eV, L3) to lower energy loss depicted the reduction of $Ni^{3+/4+}$ and the release of reactive lattice oxygen, which accounted for the generation of various oxygen-containing gases during the first exothermic reaction. At 400 ℃, the disappearance of the O K-edge pre-edge peak and the continuous shift of the Ni L-edge peak to lower energy loss corroborated the further reduction of Ni and the complete transformation of NCM811 into the rock-salt phase.

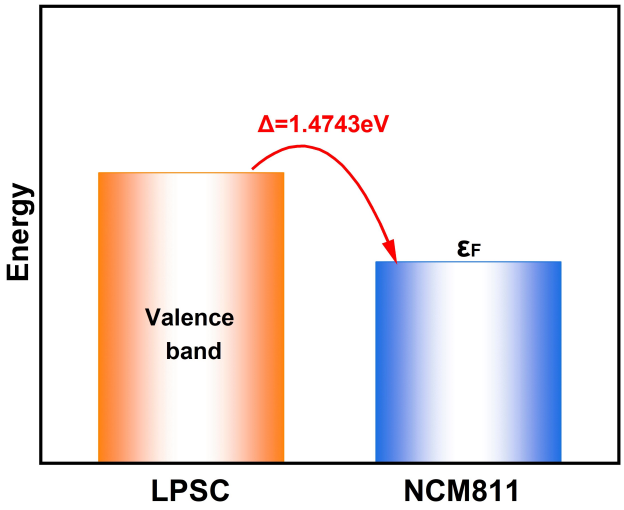

Figure S14. Schematic of oxidative degradation mechanism of a solid electrolyte in contact with a cathode active material based on band theory of solids.

The objective of this experiment is to demonstrate the inherent interfacial incompatibility between LPSC and NCM811.

The valence band maximum of LPSC lied energetically above the Fermi level of NCM811. This interfacial energy offset drives electron transferring from cathode to SE, leading to the oxidative degradation of LPSC. These findings highlight the intrinsic incompatibility at the NCM811/LPSC interface.

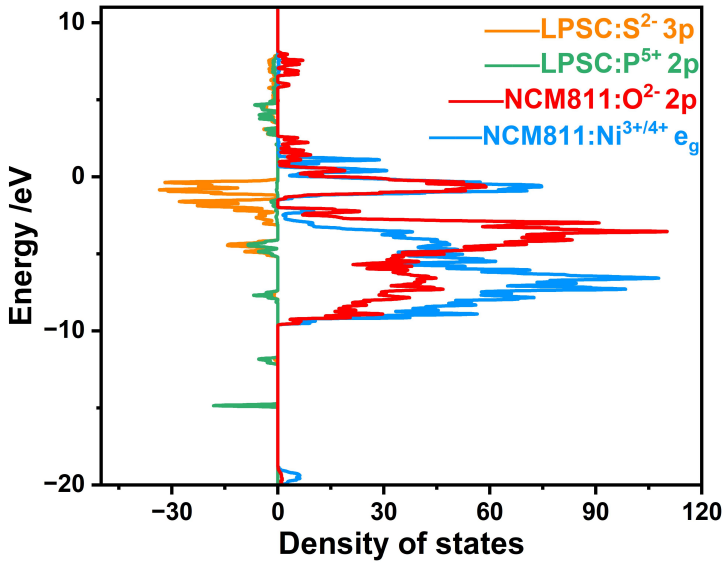

Figure S15. Densities of states (DOSs) of LPSC and NCM811.

The objective of this experiment is to demonstrate the inherent interfacial incompatibility between LPSC and NCM811.

DOS calculations revealed significant overlap between the S 3p orbitals of LPSC and the O 2p/Ni e_g orbitals of NCM811 near the Fermi level. This overlap indicates a lower energy barrier for electron exchange, further supporting the hypothesis of strong chemical incompatibility between them. Furthermore, the P 2p orbitals of LPSC also showed considerable overlap with the O 2p/Ni e_g orbitals of NCM811, suggesting a tendency for spontaneous chemical bonding.

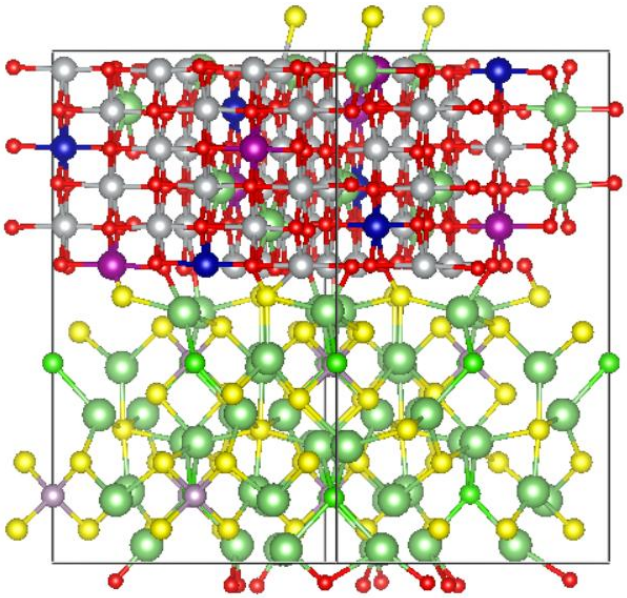

Figure S16. Delithiated NCM811 with LPSC at 25 ℃ simulated by AIMD.

The aim of this experiment is to investigate the interfacial reactions between delithiated NCM811 and LPSC.

The delithiated NCM811 and LPSC were chemically incompatible, resulting in the formation of S-O and S-Ni at the cathode/SE interface. However, the relatively slow interfacial reaction kinetics at room temperature contributed to the stability of the majority of the PS_4^{3-} structure.

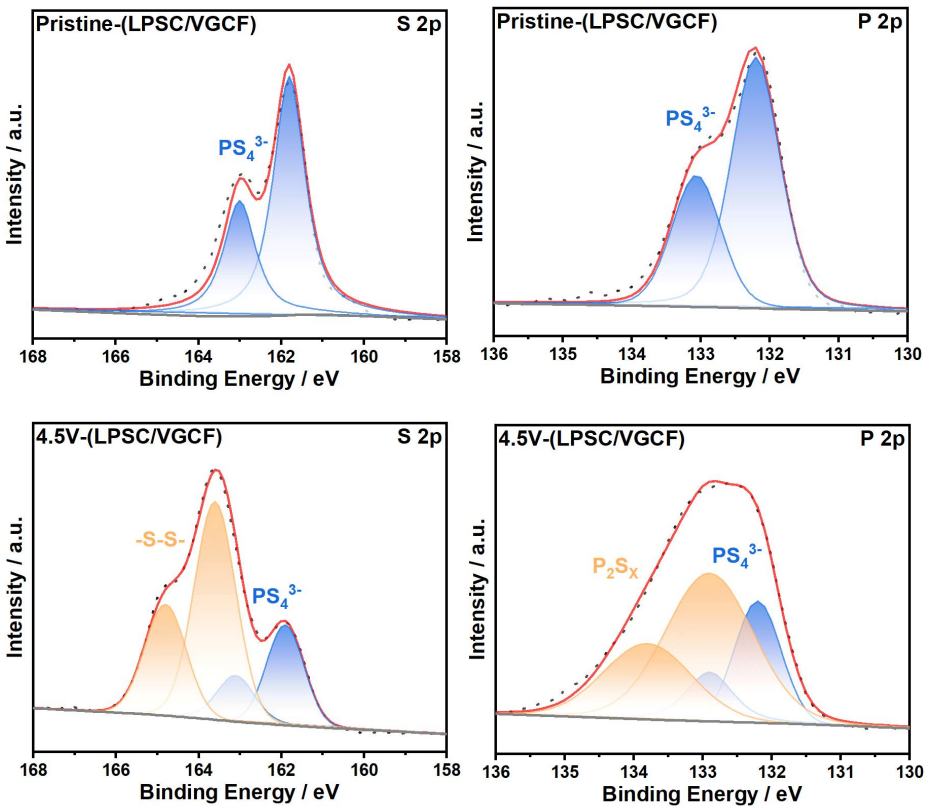

Figure S17. S 2p and P 2p XPS spectra for the LPSC/VGCF (LPSC and VGCF in a weight of 9:1) before and after being charged to 4.5 V (vs. Li^+/Li).

This experiment aims to obtain the electrochemically decomposed LPSC and demonstrate that its decomposition products align with the interphase composition of the 100% SOC composite cathode (NMC811, LPSC, and VGCF in a weight ratio of 70:30:3).

S 2p and P 2p XPS spectra revealed that after electrochemical decomposition, LPSC formed an interphase containing components such as -S-S- and -P-S-P-, consistent with the interphase composition of the 100% SOC composite cathode.

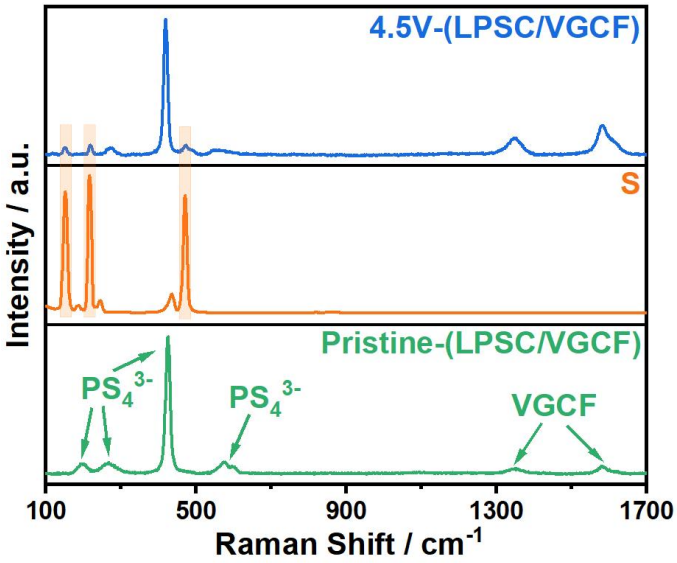

Figure S18. Raman spectra of LPSC/VGCF (LPSC and VGCF in a weight of 9:1) before and after being charged to 4.5 V (vs. Li^+/Li).

This experiment aims to obtain the electrochemically decomposed LPSC and demonstrate that its decomposition products align with the interphase composition of the 100% SOC composite cathode (NMC811, LPSC, and VGCF in a weight ratio of 70:30:3).

The characteristic peaks observed at 152 cm^{-1}, 217 cm^{-1}, and 471 cm^{-1} in Raman spectra confirmed the presence of S, which was a product of the electrochemical decomposition of LPSC under high voltage conditions. The decomposition product is consistent with the interphase composition of the 100% SOC composite cathode.

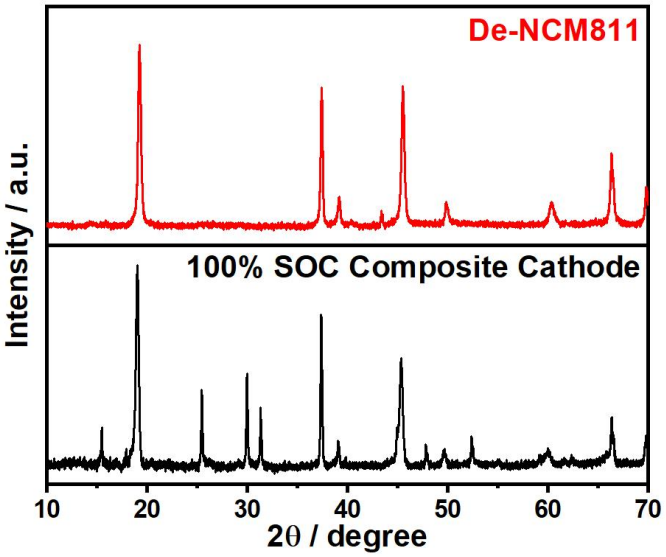

Figure S19. XRD patterns of the 100% SOC composite cathode (NMC811, LPSC, and VGCF in a weight ratio of 70:30:3) and the delithiated NCM811 (named as De-NCM) from LIBs.

The aim of this experiment is to obtain a large quantity of delithiated NCM811 from LIBs for subsequent testing.

The NCM811/LE/Gr LIBs were charged to 4.5 V (vs. Li^+/Li) at 0.05C and 30 ℃. After soaking in EC and thorough cleaning, the electrode was dried in an argon atmosphere. Finally, the cathode powders were gently scraped off the current collector and collected for subsequent testing. The delithiated NCM811 obtained from LIBs exhibited a structure similar to that of ASSBs. Therefore, it is feasible and reasonable to use this delithiated NCM811, isolated from LIBs, to investigate the interfacial reactions between it and various sulfur-containing substances (such as sulfide SEs and their electrochemical decomposition products).

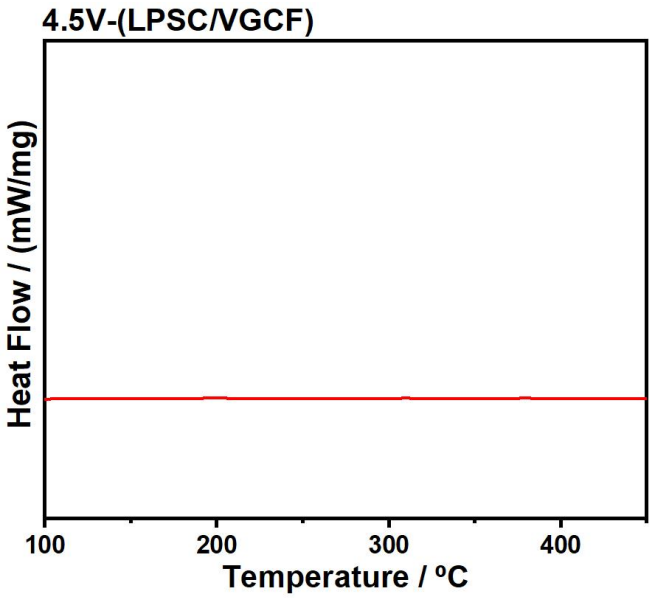

Figure S20. DSC profiles of LPSC/VGCF (LPSC and VGCF in a weight of 9:1) after being charged to 4.5 V (vs. Li^+/Li).

The aim of this experiment is to demonstrate that the heat contribution from the first exothermic peak of De-NCM/4.5V-(LPSC/VGCF) is unrelated to the decomposition reaction of 4.5V-(LPSC/VGCF) itself.

The absence of endothermic or exothermic peaks in 4.5V-(LPSC/VGCF) proved the validity of the conclusion.

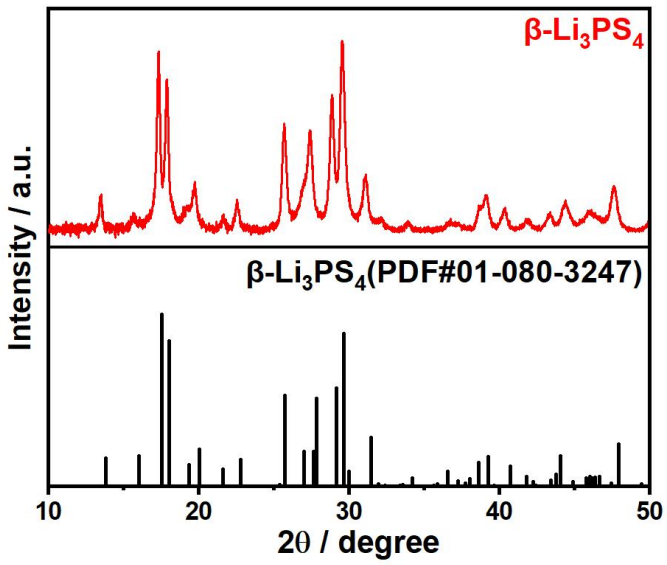

Figure S21. XRD patterns of the as-synthesized β-Li_3PS_4 samples.

The as-synthesized β-Li_3PS_4 samples are used to investigate the impact of the electrochemical decomposition products of LPSC on the exothermic behavior.

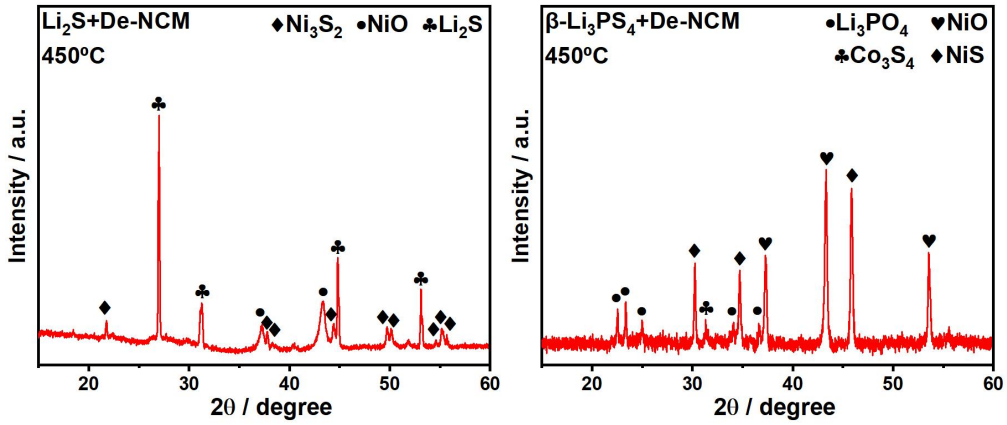

Figure S22. XRD patterns of electrochemical decomposition products of LPSC (Li_2S and β-Li_3PS_4) with delithiated NCM811 (named as De-NCM) after heating at 450 ℃.

The aim of this experiment is to identify the exothermic reaction products of electrochemical decomposition products of LPSC (Li_2S and β-Li_3PS_4) with delithiated NCM811.

After heating at 450 ℃, β-Li_3PS_4 combined with delithiated NCM811 yielded NiO, NiS, Li_3PO_4, and Co_3S_4, while Li_2S combined with delithiated NCM811 produced NiO and Ni_3S_2.

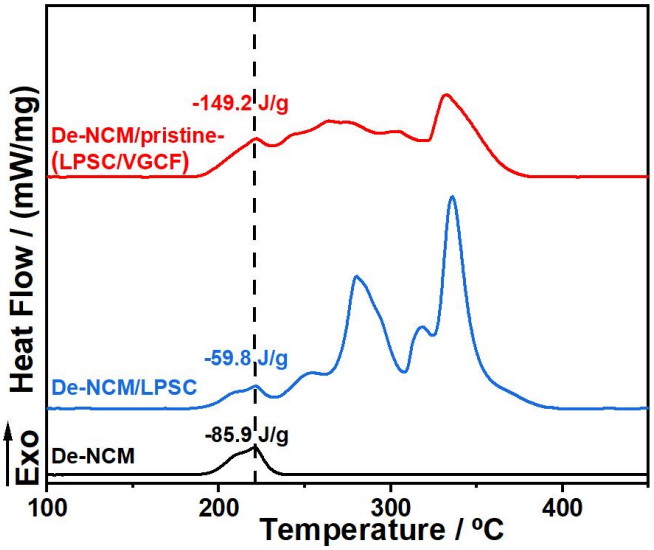

Figure S23. DSC profiles of delithiated NCM (named as De-NCM), De-NCM/LPSC (De-NCM and LPSC in a weight ratio of 7:3), and De-NCM/pristine-(LPSC/VGCF) (De-NCM, LPSC, and VGCF in a weight ratio of 70:30:3).

The purpose of this experiment is to quantify the heat contribution from the reaction between VGCF with De-NCM.

For the De-NCM, an exothermic peak was observed at 221 °C with a total enthalpy change of 85.9 $J \cdot g^{-1}$. In the case of De-NCM/LPSC, the first exothermic peak observed at 221 °C was nearly identical to that of the NCM phase transition, with a heat release of 59.8 $J \cdot g^{-1}$. The heat generated by the delithiated NCM in De-NCM/LPSC was calculated as $85.9 \times 0.7 = 60.1$ $J \cdot g^{-1}$, which was almost identical to the observed 59.8 $J \cdot g^{-1}$. These findings indicate that LPSC and delithiated NCM do not react during the first exothermic process. For De-NCM/(LPSC/VGCF), the first exothermic peak remained unchanged at 221 °C, but the enthalpy change increased to 149.2 $J \cdot g^{-1}$. Here, the NCM contributes 58.4 $J \cdot g^{-1}$ ($85.9 \times 70 / 103$ $J \cdot g^{-1}$), while the remaining 90.8 $J \cdot g^{-1}$ could be attributed to the heat released by VGCF during the generation of CO_2 and CO.

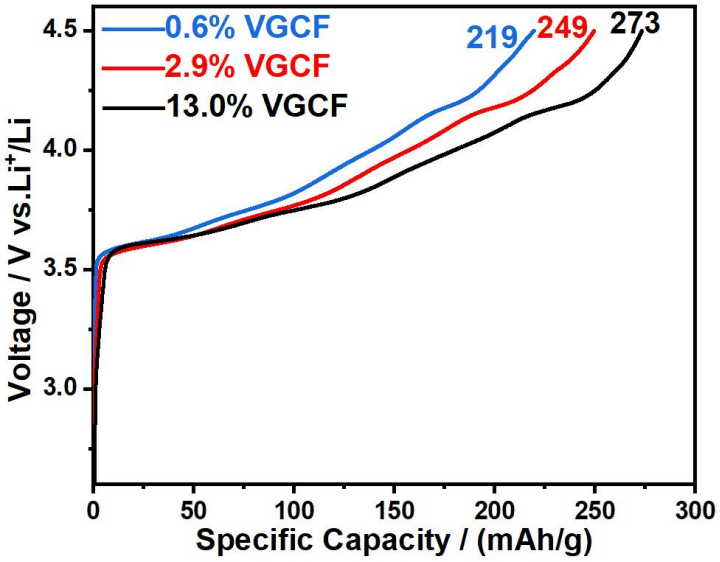

Figure S24. Typical charge curves of the cell of NCM811/LPSC/Li-In with different wt% of VGCF (carbon additive) after charging to 4.5 V (vs. Li^+/Li) at 0.1C and 30 ℃.

The aim of this experiment is to prepare three 100% SOC composite cathodes with different VGCF wt% for thermal runaway testing, in order to investigate the influence of VGCF on thermal propagation mechanisms.

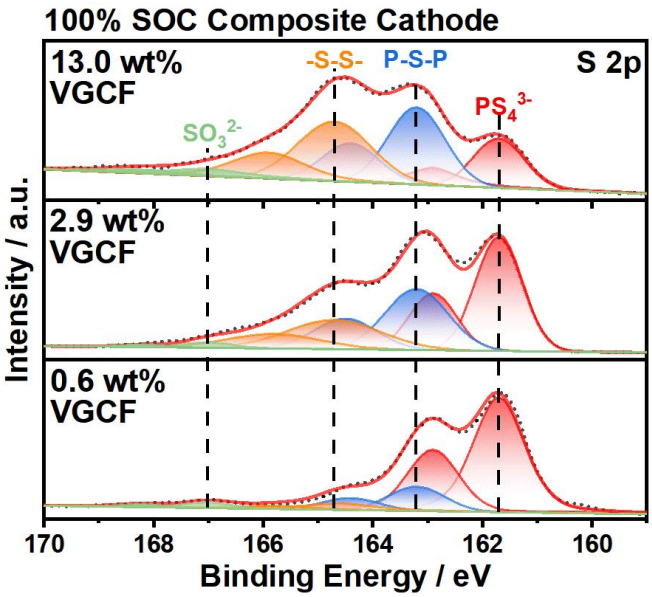

Figure S25. S 2p XPS spectra of the 100% SOC composite cathodes with different wt% of VGCF (carbon additive).

The aim of this experiment is to demonstrate that the presence of VGCF can promote the electrochemical decomposition of LPSC.

As the VGCF content increased, the intensity of -S-S- and -P-S-P- also increased in the 100% SOC composite cathode, indicating that VGCF promoted the decomposition of LPSC to form -S-S- and bridge sulfur species.

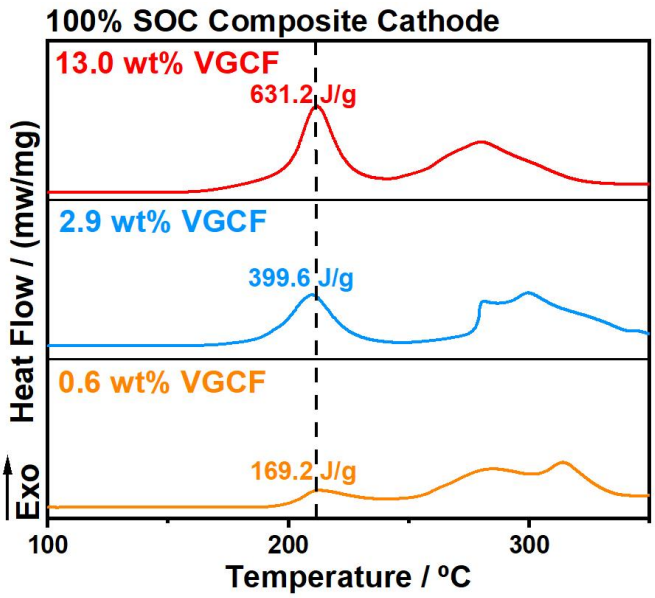

Figure S26. DSC curves of the 100% SOC composite cathodes with different wt% of VGCF (carbon additive).

The aim of this experiment is to investigate the impact of the presence of VGCF on the exothermic reactions.

As the VGCF content increased, enthalpy changes of the first exothermic peak increased to 169.2 $J \cdot g^{-1}$, 399.6 $J \cdot g^{-1}$, and 631.2 $J \cdot g^{-1}$. These findings confirme two synergistic thermal pathways: (1) direct exothermic carbon-cathode reactions generating CO/CO_2, and (2) catalytic acceleration of LPSC decomposition that amplifies subsequent interfacial exothermicity. This dual mechanism establishes conductive carbon as both reactant and reaction promoter in thermal runaway initiation.

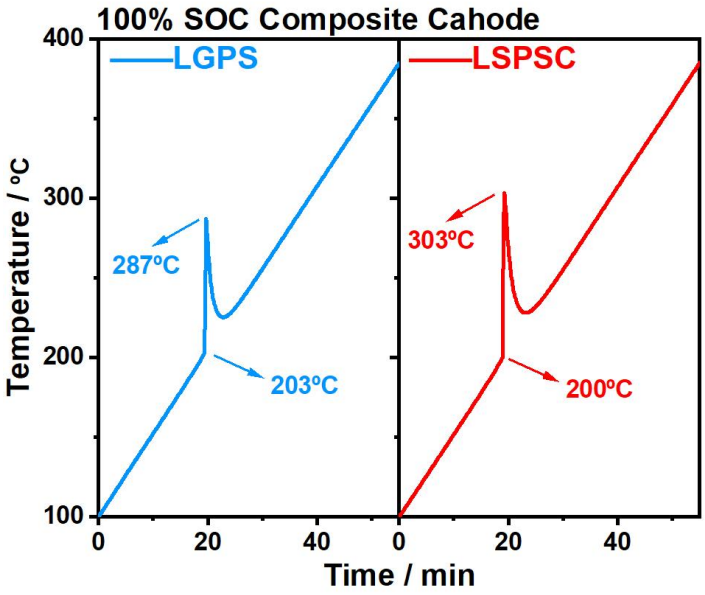

Figure 27. Adiabatic ramp test thermal profiles of the 100% SOC LGPS and LSPSC composite cathodes (NMC811, SE, and VGCF in a weight ratio of 70:30:3) at a scanning rate of 5 °C min^{-1} in ARC.

This experiment aims to investigate the thermal runaway behaviors of the 100% SOC LGPS and LSPSC composite cathodes under a constant heating rate of 5 °C min^{-1}.

100% SOC LGPS composite cathode exhibited severe self-heating, with the sample temperature rapidly increases to 287 °C at 203 °C. And 100% SOC LSPSC composite cathode also exhibited severe self-heating, with the sample temperature rapidly increases to 287 °C at 203 °C. These indicate that thermal abuse can trigger thermal runaway in these composite cathodes.

Additionally, the 100% SOC LPSC (**Figure S4**), LGPS, and LSPSC composite cathodes all exhibited significant severe self-heating around 200°C, suggesting that this phenomenon may be caused by the same underlying mechanism. We will further investigate this in subsequent studies.

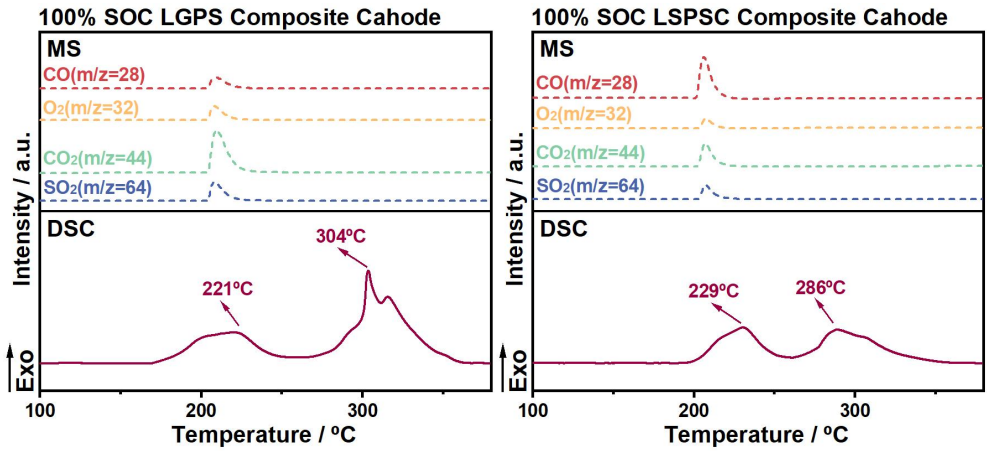

Figure S28. DSC and MS profiles of the 100% SOC LGPS and LSPSC composite cathodes (NMC811, SE, and VGCF in a weight ratio of 70:30:3).

The aim of this experiment is to investigate the exothermic and gas-generation behaviors of the 100% SOC LGPS and LSPSC composite cathodes.

The enthalpy changes of the first exothermic reaction for the 100% SOC LGPS and LSPSC composite cathodes were 320.7 $J \cdot g^{-1}$ and 346.4 $J \cdot g^{-1}$, respectively, accompanied by the generation of SO_2.

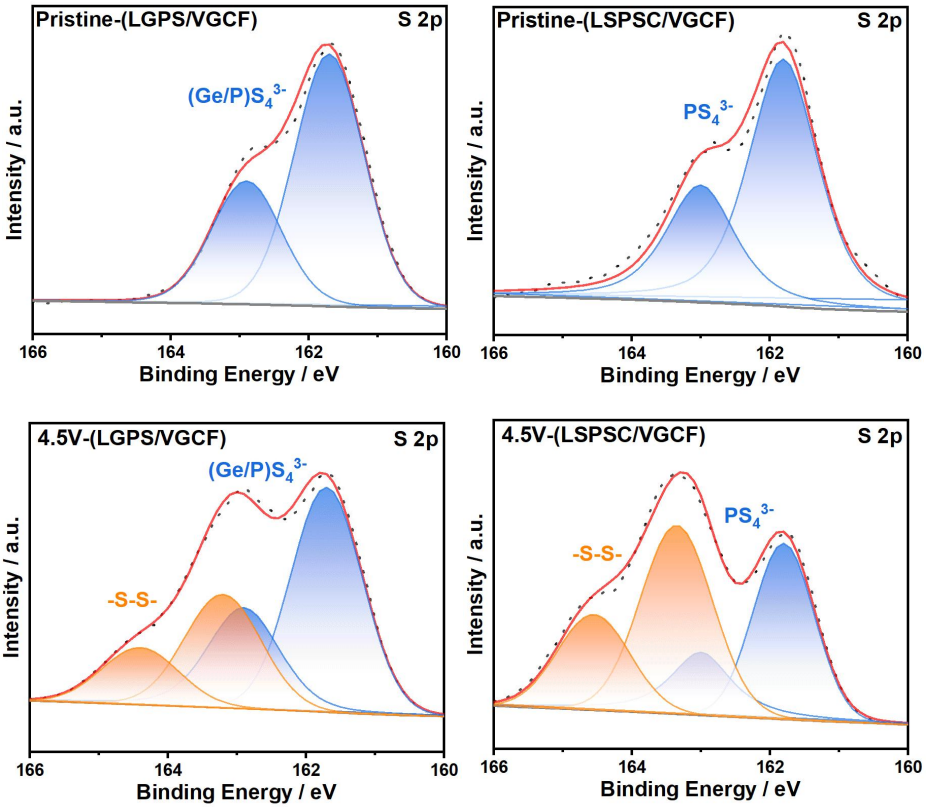

Figure S29. S 2p XPS spectra for the LGPS/VGCF (LGPS and VGCF in a weight of 9:1) and LSPSC/VGCF (LSPSC and VGCF in a weight of 9:1) before and after charging to 4.5V (vs. Li^+/Li).

This experiment aims to obtain the electrochemically decomposed LGPS and LSPSC.

Similar to LPSC (**Figure S17**), both types of SEs also produced decomposition products such as -S-S- and -P-S-P- after electrochemical decomposition.

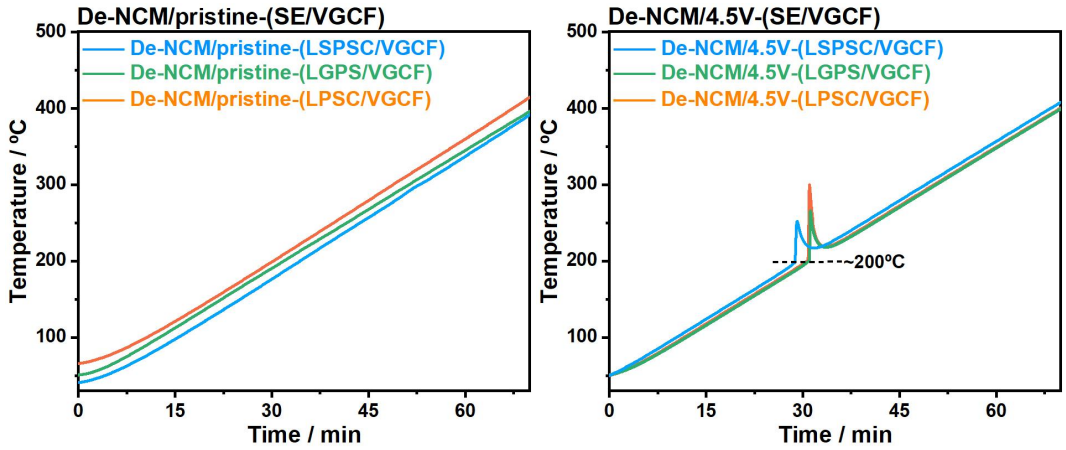

Figure 30. Adiabatic ramp test thermal profiles of delithiated-NCM (De-NCM)/pristine-(SE/VGCF) and De-NCM/4.5V-(SE/VGCF) at a scanning rate of 5 °C min^{-1} in ARC.

The objective of this experiment is to demonstrate that the severe self-heating behavior observed in 100% SOC LPSC, LGPS, and LSPSC composite cathodes around 200 °C is caused by the electrochemical decomposition of SEs.

Severe self-heating behavior were detected near 200 °C in the ramp test of De-NCM/4.5V-(SE/VGCF), which corresponded to the temperature observed in the 100% SOC LPSC (**Figure S4**), LGPS (**Figure S27**), and LSPSC (**Figure S27**) composite cathodes, whereas no such phenomenon occured in De-NCM/pristine-(SE/VGCF). These fingdings suggest that the electrochemical decomposition of SEs induces severe self-heating in the 100% SOC LPSC, LGPS, and LSPSC composite cathodes, which is the primary cause of the earlier and more intense exothermic behavior of the sample.

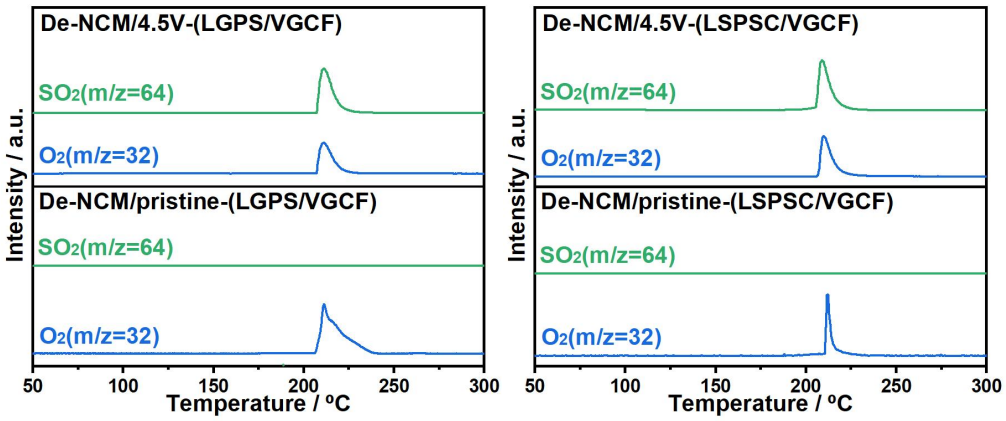

Figure S31. MS profiles of delithiated-NCM(De-NCM)/pristine-(SE/VGCF) and De-NCM/4.5V-(SE/VGCF).

The objective of this experiment is to demonstrate that the generation of SO_2 during the heating process of the 100% SOC LGPS and LSPSC composite cathodes is caused by the electrochemical decomposition of LGPS and LSPSC.

No SO_2 generation was detected in De-NCM/pristine-(LGPS/VGCF) and De-NCM/pristine-(LSPSC/VGCF), whereas SO_2 was detected in De-NCM/4.5V-(LGPS/VGCF) and De-NCM/4.5V-(LSPSC/VGCF), indicating that the introduction of the electrochemical decomposition of LGPS and LSPSC led to the generation of SO_2.

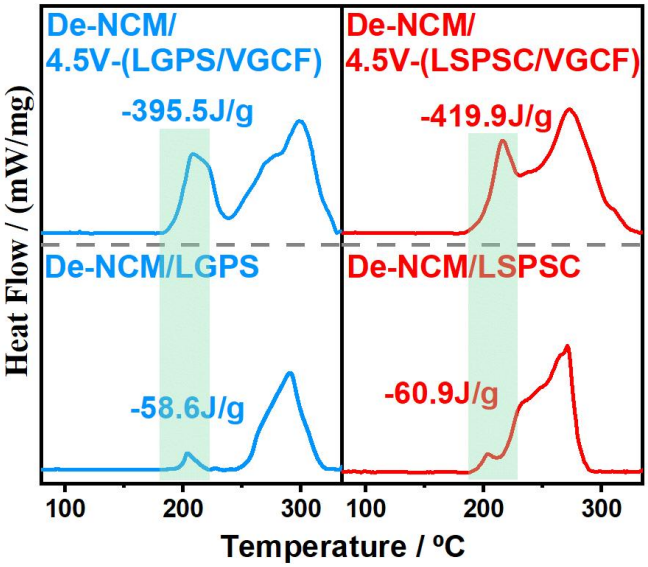

Figure S32. DSC profiles of the delithiated NCM811(De-NCM)/LGPS (De-NCM and LGPS in a weight ratio of 7:3), De-NCM/LSPSC (De-NCM and LSPSC in a weight ratio of 7:3), De-NCM/4.5V-(LGPS/VGCF) (De-NCM, LGPS, and VGCF in a weight ratio of 70:30:3), and De-NCM/4.5V-(LSPSC/VGCF) (De-NCM, LSPSC, and VGCF in a weight ratio of 70:30:3).

The purpose of this experiment is to investigate whether a reaction occurs between De-NCM and SEs (LGPS and LSPSC) during the first exothermic process, as well as to explore the influence of the electrochemical decomposition of SEs (LGPS and LSPSC) on the heat release.

For De-NCM/LGPS and De-NCM/LSPSC, the enthalpy changes of the first exothermic process were 58.6 $J \cdot g^{-1}$ and 60.9 $J \cdot g^{-1}$, respectively. In previous studies, we have demonstrated that the heat released by the phase transition of De-NCM in De-NCM/SE (De-NCM and SE in a weight ratio of 7:3) is approximately 60.1 $J \cdot g^{-1}$ (**Figure S23**). This value closely matches the enthalpy changes observed for De-NCM/LGPS and De-NCM/LPSC during the first exothermic process. These results indicate that SEs (LGPS and LPSC) and delithiated NCM do not react during the first exothermic process.

For De-NCM/4.5V-(LGPS/VGCF) and De-NCM/(LSPSC/VGCF), the enthalpy changes of the first exothermic process were 395.5 $J \cdot g^{-1}$ and 419.9 $J \cdot g^{-1}$, respectively.

In previous studies, we have demonstrated that in the De-NCM/(SE/VGCF), the heat released by the phase transition of De-NCM is approximately 58.4 $J \cdot g^{-1}$ (**Figure S23**), and the heat released by the reaction between VGCF and delithiated NCM is 90.8 $J \cdot g^{-1}$ (**Figure S23**). Similarly, in the De-NCM/4.5V-(SE/VGCF) system, these two contributions remain unchanged. Therefore, in De-NCM/4.5V-(LGPS/VGCF), the additional 246.3 $J \cdot g^{-1}$ (395.5 - 60.1 - 90.8 $J \cdot g^{-1}$) of heat release is attributed to the exothermic reaction between the electrochemical decomposition products of LGPS and De-NCM. In De-NCM/4.5V-(LSPSC/VGCF), the additional 270.7 $J \cdot g^{-1}$ (419.9 - 58.4 - 90.8 $J \cdot g^{-1}$) of heat release is attributed to the exothermic reaction between the electrochemical decomposition products of LSPSC and De-NCM. These results indicate that in both De-NCM/4.5V-(LGPS/VGCF) and De-NCM/(LPSC/VGCF), the first exothermic process is dominated by the reaction between the electrochemical decomposition products of the sulfide SEs and NCM811. These findings highlight the significant influence of electrochemical processes on thermal runaway.

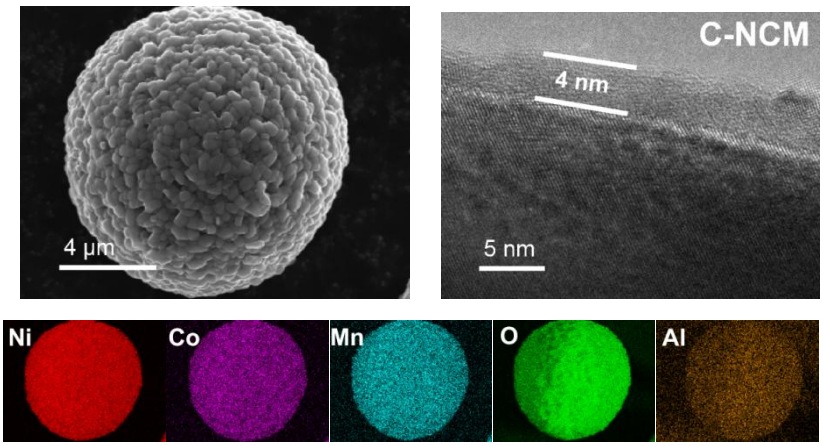

Figure S33. Typical surface SEM-EDS and TEM images of Al_2O_3 coated $LiNi_{0.8}Co_{0.1}Mn_{0.1}O_2$ (named as C-NCM) samples.

It was observed by TEM imaging that the thickness of Al_2O_3 coating was 4 nm and coating homogeneous.

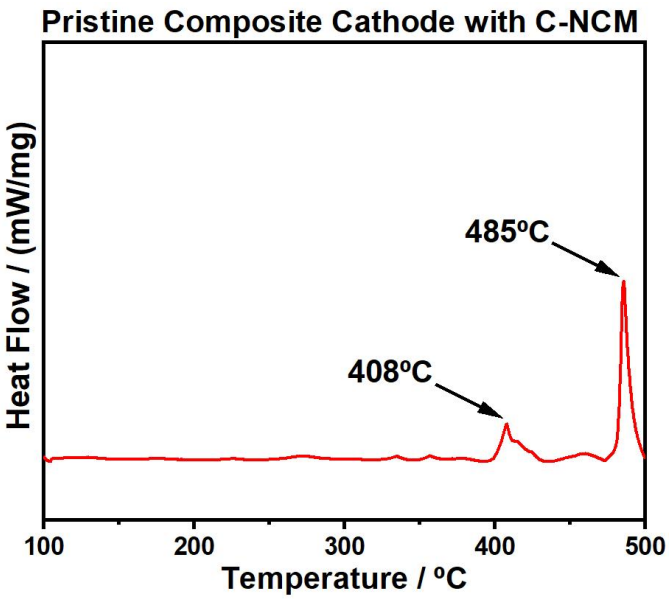

Figure S34. DSC profiles of the pristine composite cathode (Al_2O_3 coated NCM811 (named as C-NCM), LPSC, and VGCF in a weight ratio of 70:30:3).

The objective of this experiment is to demonstrate, from a thermochemical stability perspective, that the interfacial compatibility between C-NCM and LPSC is superior to that between NCM (bare NCM811) and LPSC.

The two exothermic peaks of the pristine composite cathode composed of C-NCM (C-NCM, LPSC, and VGCF in a weight ratio of 70:30:3) (408 ℃ and 485 ℃) were delayed compared to that of NCM (bare NCM811) (373 ℃ and 465 ℃, **Figure 1c**). The higher reaction temperature indicates that the Al_2O_3 coating enhances the interfacial compatibility between layered oxide cathode and LPSC.

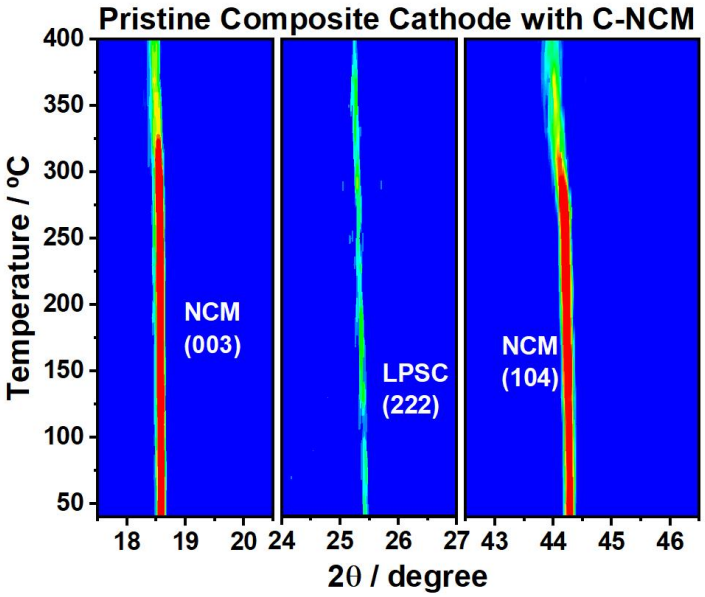

Figure S35. In situ heating XRD characterization of the pristine composite cathode (Al_2O_3 coated NCM811 (named as C-NCM), LPSC, and VGCF in a weight ratio of 70:30:3).

The objective of this experiment is to demonstrate, from a thermochemical stability perspective, that the interfacial compatibility between C-NCM and LPSC is superior to that between NCM (bare NCM811) and LPSC.

In the pristine composite cathode system composed of C-NCM, no distinct NiO characteristic signals were observed when heated to 400 °C. In contrast, the pristine composite cathode system composed of bare NCM exhibits strong NiO characteristic signals when heated to around 373 °C (**Figure 1d**). The higher reaction temperature indicates that the Al_2O_3 coating enhances the interfacial compatibility between layered oxide cathode and LPSC.

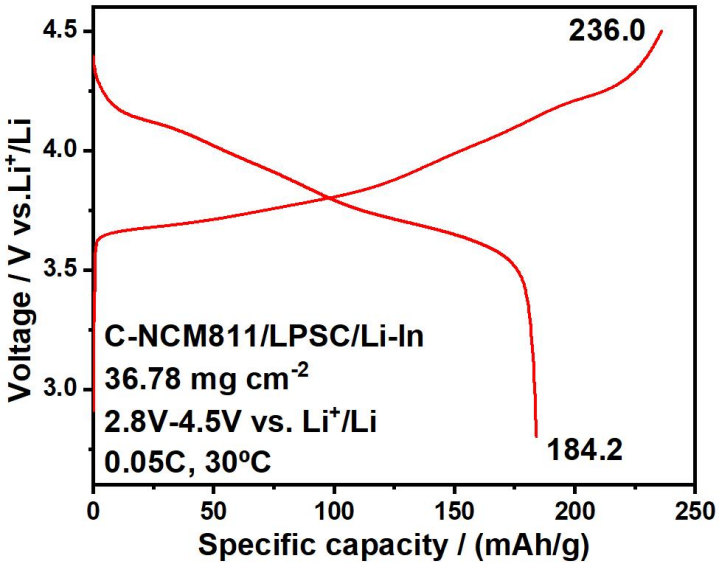

Figure S36. Typical charge-discharge curves of the cell of Al_2O_3 coated NCM811 (named as C-NCM)/LPSC/Li-In in the voltage range of 2.8-4.5 V (vs. Li^+/Li) at 0.05C and 30 ℃.

The ASSBs obtained from this experiment are used for thermal runaway testing.

The as-obtained cells delivered an initial charge specific capacity of 236.0 $mAh \cdot g^{-1}$ and an initial discharge specific capacity of 184.2 $mAh \cdot g^{-1}$.

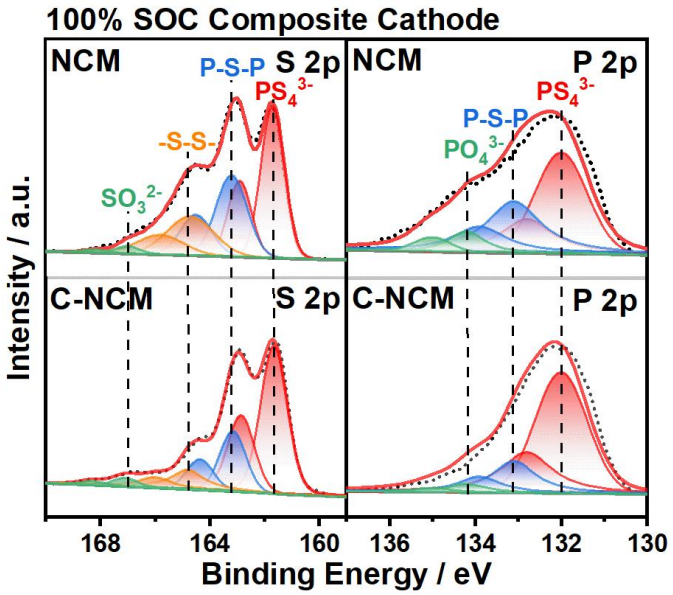

Figure S37. S 2p and P 2p XPS spectra of the 100% SOC composite cathode (layered oxide cathode, LPSC, and VGCF in a weight ratio of 70:30:3) with Al_2O_3 coated NCM811 (named as C-NCM) and NCM (bare NCM811).

The aim of this experiment is to demonstrate that the Al_2O_3 coating layer can effectively alleviate the electrochemical decomposition of LPSC.

The 100% SOC composite cathode with C-NCM presented weaker signals of -S-S-, -P-S-P-, and PO_4^{3-} compared to those detected from NCM, further confirming Al_2O_3-coated NCM811 effectively alleviated the electrochemical degradation of LPSC.

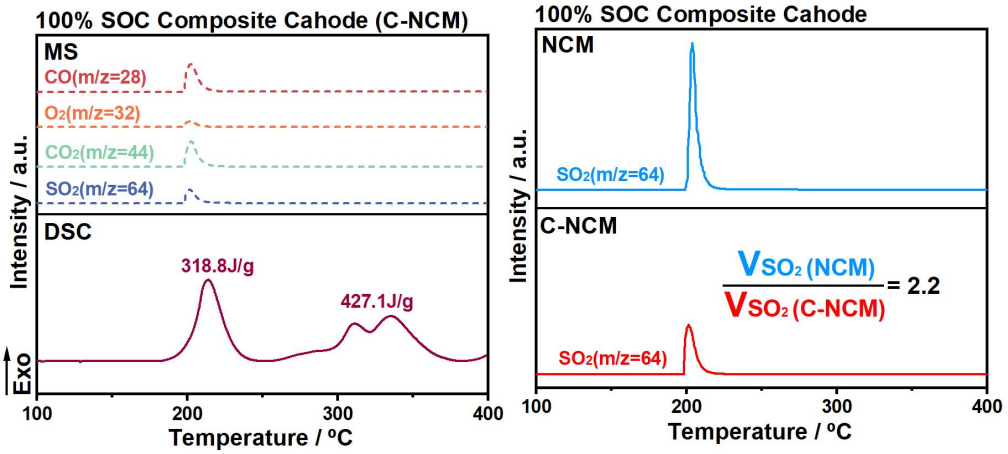

Figure S38. DSC and MS profiles of the 100% SOC composite cathode (Al_2O_3 coated NCM811 (named as C-NCM), LPSC, and VGCF in a weight ratio of 70:30:3), and SO_2 evolution of the 100% SOC composite cathode with C-NCM and NCM (bare NCM811).

The aim of this experiment is to investigate whether the Al_2O_3 coating can enhance the thermal safety of the composite cathode system.

For the 100% SOC C-NCM composite cathode, DSC result exhibited that the first exothermic peak appears at 213 °C, with an enthalpy change of 318.8 $J \cdot g^{-1}$, superior to the 209 °C and 399.6 $J \cdot g^{-1}$ from B-NCM composite cathode, respectively.

We maintained identical mass for both composite cathodes and the same flow rate of the purge gas throughout the testing process. By integrating the gas signal intensity over time, we compared the amount of SO_2 gas released. The SO_2 release from the 100% SOC composite cathode composed of NCM (bare NCM) was 2.2 times that of the 100% SOC composite cathode composed of C-NCM. The Al_2O_3 coating reduced heat release and SO_2 gas generation to some extent.

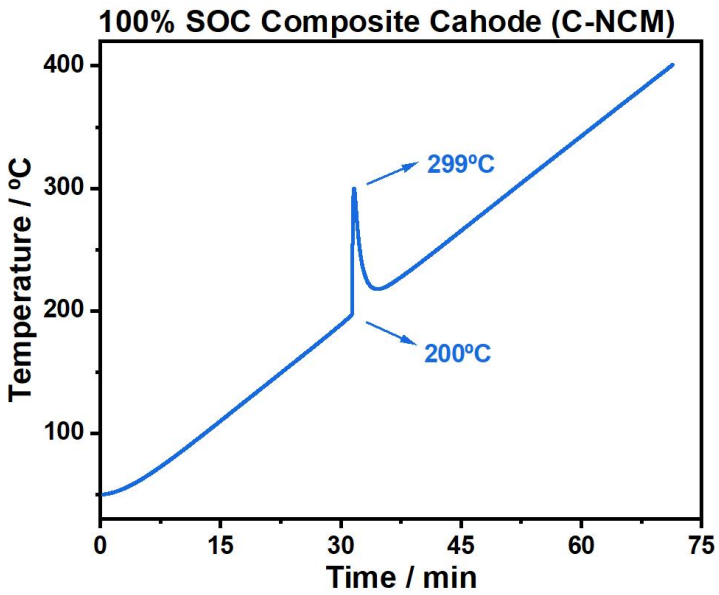

Figure S39. Adiabatic ramp test thermal profiles of the 100% SOC composite cathode (Al_2O_3 coated NCM811 (named as C-NCM), LPSC, and VGCF in a weight ratio of 70:30:3) under a constant heating rate of 5 ℃ min^{-1} in ARC.

This experiment aims to investigate whether the Al_2O_3 coating can address the thermal safety issue of severe self-heating around 200 ℃ in the 100% SOC composite cathode.

Unfortunately, the 100% SOC composite cathode composed of C-NCM still exhibited severe self-heating characteristics during the ramp test, with the sample temperature rapidly increases to 200 ℃ at 299 ℃. Even with the Al_2O_3 coating, it is not possible to completely suppress the severe thermal runaway induced by the electrochemical decomposition of LPSC.

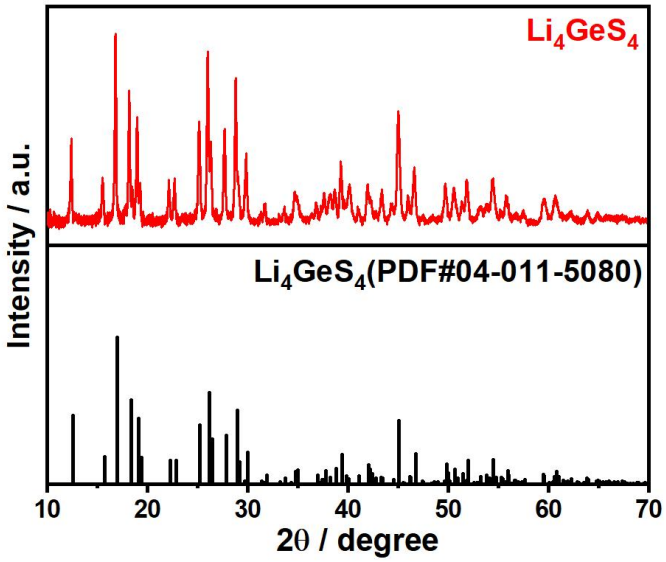

Figure S40. XRD patterns of the as-synthesized Li_4GeS_4 samples.

The as-synthesized LGS samples are used as the conductive additive in the composite cathode (NMC811, LGS, and VGCF in a weight ratio of 70:30:3).

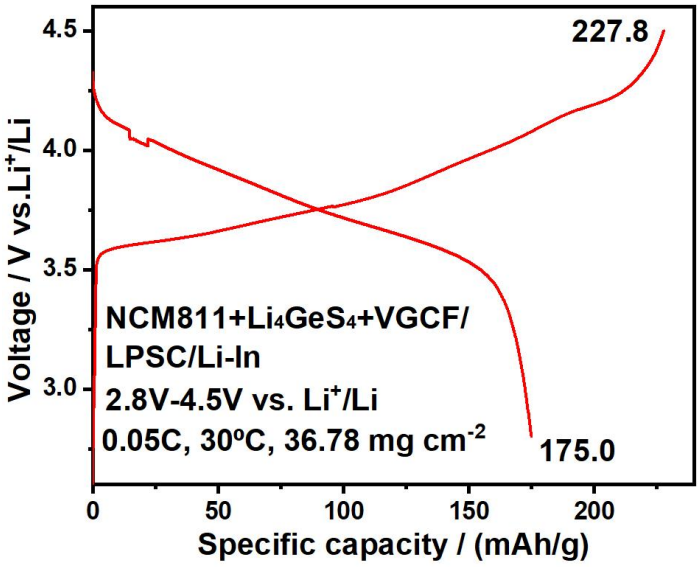

Figure S41. Typical charge-discharge profiles of LGS-NCM811/LPSC/Li-In cells in the voltage range of 2.8−4.5 V (vs. Li^+/Li) at 0.05C and 30 ℃.

The ASSBs obtained from this experiment are used for thermal runaway testing.

The as obtained cells delivered an initial charge specific capacity of 227.8 $mAh \cdot g^{-1}$ and an initial discharge specific capacity of 175.0 $mAh \cdot g^{-1}$.

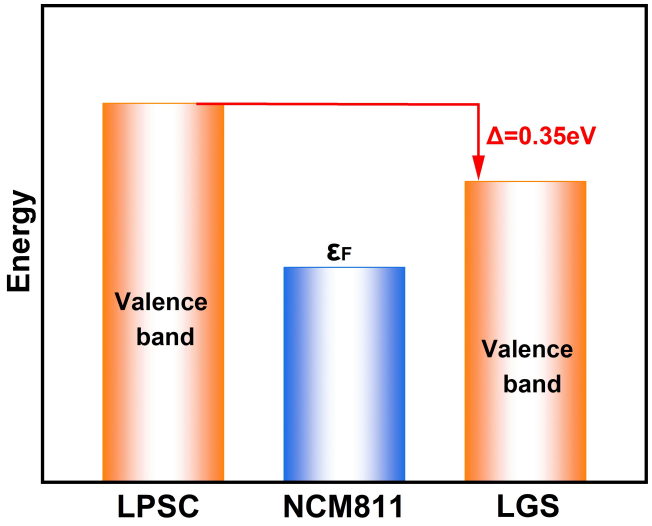

Figure S42. Schematic of oxidative degradation mechanism of sulfide SEs (LPSC and LGS) in contact with cathode active material (NCM811) based on band theory of solids.

The purpose of this experiment is to demonstrate that the compatibility of LGS/NCM811 is superior to that of LPSC/NCM811.

LGS successfully reduced the gap between the valence band maximum of the sulfide solid electrolyte and the Fermi level of NCM811, validating the Ge-substitution strategy for interfe optimization.

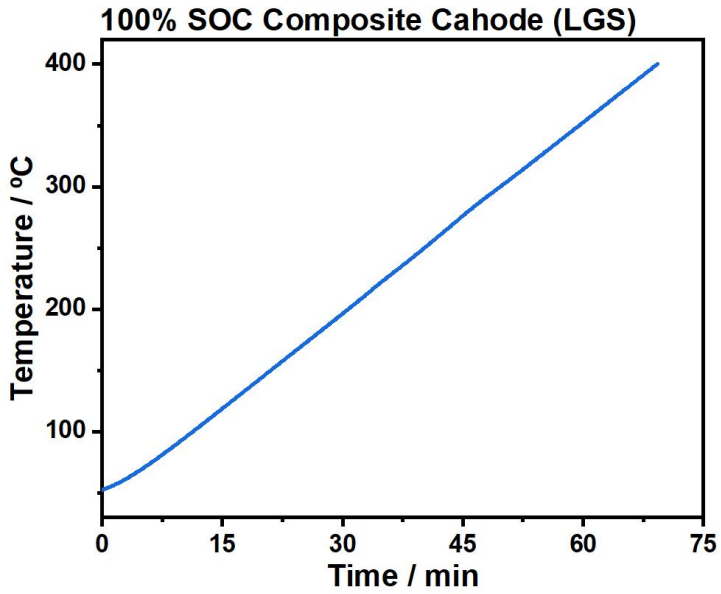

Figure S43. Adiabatic ramp test thermal profiles of the 100% SOC LGS composite cathode (NMC811, LGS, and VGCF in a weight ratio of 70:30:3) under a constant heating rate of 5 °C min^{-1} in ARC.

This experiment aims to investigate whether the LGS can address the thermal safety issue of severe self-heating around 200 °C in the 100% SOC composite cathode.

Clearly, no severe self-heating was observed in the 100% SOC LGS composite cathode, indicating that LGS completely suppressed the severe thermal runaway induced by the electrochemical decomposition of sulfide SE, validating the Ge-substitution strategy for interfe optimization.